ACS Biomaterials SCIENCE & ENGINEERING

pubs.acs.org/journal/abseba

Article

High-Performance Implantable Sensors based on Anisotropic Magnetoresistive $La_{0.67}Sr_{0.33}MnO_3$ for Biomedical Applications

Arturo Vera, Isidoro Martínez, Luiz Guilherme Enger, Bruno Guillet, Rubén Guerrero, José Manuel Diez, Olivier Rousseau, Marc Lam Chok Sing, Victor Pierron, Paolo Perna, Jaime J. Hernández, Isabel Rodríguez, Ivo Calaresu, Anja Meier, Carmen Huck, Ana Domínguez-Bajo, Ankor González-Mayorga, Elisa López-Dolado, María C. Serrano, Laura Ballerini, Lucas Pérez, Rodolfo Miranda, Stéphane Flament, María Teresa González,* Laurence Méchin, and Julio Camarero

Cite This: *ACS Biomater. Sci. Eng.* 2023, 9, 1020–1029

Read Online

ACCESS | Metrics & More | Article Recommendations | Supporting Information

ABSTRACT: We present the design, fabrication, and characterization of an implantable neural interface based on anisotropic magnetoresistive (AMR) magnetic-field sensors that combine reduced size and high performance at body temperature. The sensors are based on $La_{0.67}Sr_{0.33}MnO_3$ (LSMO) as a ferromagnetic material, whose epitaxial growth has been suitably engineered to get uniaxial anisotropy and large AMR output together with low noise even at low frequencies. The performance of LSMO sensors of different film thickness and at different temperatures close to 37 °C has to be explored to find an optimum sensitivity of ∼400%/T (with typical detectivity values of 2 nT·Hz$^{-1/2}$ at a frequency of 1 Hz and 0.3 nT·Hz$^{-1/2}$ at 1 kHz), fitted for the detection of low magnetic signals coming from neural activity. Biocompatibility tests of devices consisting of submillimeter-size LSMO sensors coated by a thin poly(dimethyl siloxane) polymeric layer, both *in vitro* and *in vivo*, support their high suitability as implantable detectors of low-frequency biological magnetic signals emerging from heterogeneous electrically active tissues.

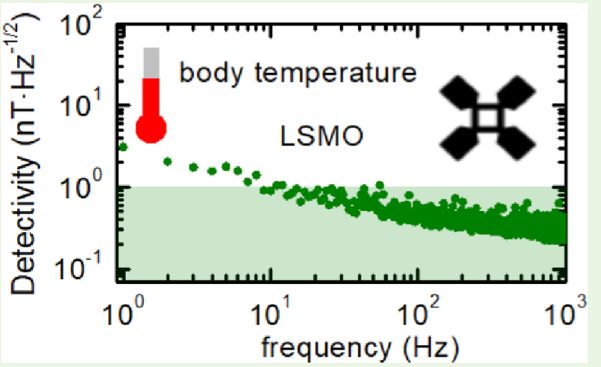

KEYWORDS: *anisotropic magnetoresistance, magnetic sensors, neural interfaces, thin film oxide, detectivity measurements, in vitro and in vivo biocompatibility*

INTRODUCTION

The use of spintronic-based devices for magnetic detection has been extensively studied in the last decades.[1−6] In particular, anisotropic magnetoresistive (AMR), giant magnetoresistive (GMR), and tunnel magnetoresistive (TMR) technologies are currently used in the fabrication of magnetic sensors integrated in different applications because of their low fabrication cost, robustness, temperature stability, and scalability.[7] To obtain a high signal-to-noise ratio for applications, the noise characterization is essential. For the detection of magnetic signals of low frequency (f), the $1/f$ noise, always present in any device, is particularly relevant and can become too high. Here, AMR sensors become competitive when compared with TMR and GMR ones due to their particularly low $1/f$ noise.[8,9] Moreover, TMR and GMR spintronic devices involve a much more complex fabrication than AMR ones, as the latter can be composed of a single material tailored on top of a substrate, making this technology highly suitable for industrial implementation. Indeed, there is a continuous investigation to improve the performance of magnetic field sensors by different means.[10−13]

In the last years, magnetic devices have been progressively incorporated to biomedical technologies. These new biomagnetic techniques will benefit from the fact that magnetic fields can be recorded at a certain distance from its source and do not rely on a good electric coupling of the tissue with the sensor, in contrast to current electric techniques. Therefore, they could be much less invasive. In addition, magnetic field sensors are sensitive to the direction as well as the magnitude of the magnetic field, providing more complex and complete information of the biological signals. In this context, superconducting quantum interference device magnetometers are currently used for recording neural activity in the brain (magnetoencephalography)[14] and the cervical spinal cord (magnetospinography).[15] Optically pumped magnetometers

Received: September 30, 2022
Accepted: January 9, 2023
Published: January 31, 2023

https://doi.org/10.1021/acsbiomaterials.2c01147
ACS Biomater. Sci. Eng. 2023, 9, 1020−1029

are also proposed for magnetoencephalography.[16] Although very promising for clinical applications in diagnosis, all these devices are bulky and have working temperatures significantly different from the body temperature and, hence, are nonportable and do not allow chronical implantation. Spintronic-based devices are easily miniaturized and, therefore, they are the most suitable candidates for such applications. In particular, neuronal activity has been already recorded *in vivo* using GMR-based sensors.[17,18] AMR-based sensors are easier to fabricate and integrate. Typically, they use polycrystalline ferromagnetic permalloy (Py) films with uniaxial magnetic anisotropy induced by exchange bias or shape due to the high AMR ratio and aluminum barber poles to linearize the sensor response. Recent studies using Py AMR-based sensors report sensitivities of 500%/T[13] and 400%/T[11] at room temperature. These features highlight the potential of AMR sensors for especially demanding applications such as the detection of biomagnetic signals.

In particular, $La_{0.67}Sr_{0.33}MnO_3$ (LSMO) is a promising candidate for magnetic field sensors dedicated to biomedical applications[19] since it is a ferromagnetic material with a Curie temperature, T_c (temperature at which the material changes from ferromagnetic state to paramagnetic state), of about 77 °C, thus presenting magnetoresistive behavior at body temperature, and, more interestingly, their $1/f$ noise is very low.[20] Although its sensitivity is not as high as those based on Py, its detectivity, which establishes the ultimate noise floor of the device, can, therefore, reach very low values (see Supporting Information for the mathematical definitions of sensitivity and detectivity).[19] In this work, we present the fabrication and broad study of high-performance LSMO-based magnetic sensors as implantable neural interfaces, which present detectivity values down to 2 $nT{\cdot}Hz^{-1/2}$ at 1 Hz and 0.3 $nT{\cdot}Hz^{-1/2}$ in the white noise region, thus reaching the sub-nanoTesla regime in most of the spectra. The LSMO epitaxial growth has been suitably engineered to get uniaxial anisotropy and large AMR output around zero applied field without the need of barber poles. We report on the temperature- and magnetic field-dependent characterization of the sensors, as well as their *in vitro* and *in vivo* biocompatibility and stability when coated with a polymeric layer. The LSMO films were epitaxially grown on top of (001)-oriented $SrTiO_3$ (STO) single crystal substrates whose surfaces were on-purpose designed with a 4° miscut, named vicinal substrates. With this fabrication procedure, uniaxial anisotropy with the easy magnetization axis along the surface step edges were previously engineered.[21,22] In order to find the optimal sensor performance, we have measured sensors with different LSMO thicknesses ranging from 30 to 90 nm by means of Magneto-optic Kerr effect (MOKE) magnetometry and the magnetoresistive response in Wheatstone bridges (WB). Additional biocompatibility and stability tests of the sensors protected by a poly(dimethyl siloxane) (PDMS) coating have been carried out *in vitro* and *in vivo* up to 2 months in order to assess the potential of these sensors for implantable biomagnetic detection applications.

MATERIALS AND METHODS

Device Fabrication. The LSMO thin films were grown by pulsed laser deposition at an energy density of 1.7 $J{\cdot}cm^{-2}$ from a stoichiometric target onto vicinal STO single crystal substrates with a miscut angle of 4°, at 730 °C with an oxygen pressure of 0.2 mbar. After deposition, the LSMO films were covered by a gold layer of about 150 nm in thickness, and UV photolithography followed by wet etching in KI was performed to define four electrical contacts. The sensor active area was then delimited in the LSMO layer as shown in the schematic in Figure 1a after a second UV photolithography step,

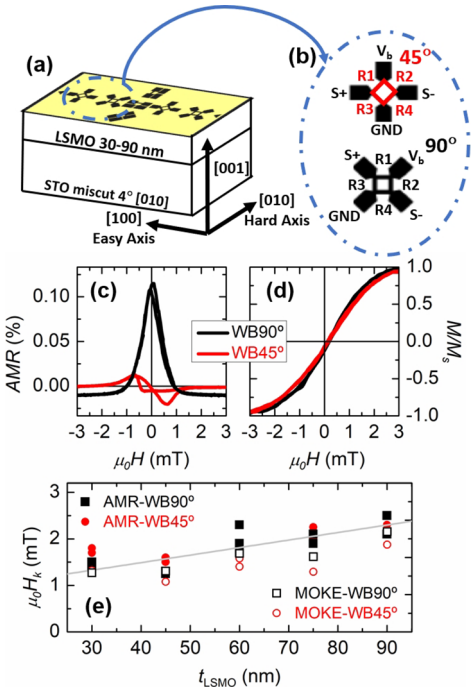

Figure 1. WB sensor configurations and representative transport and magnetic characterization. (a) Typical sample of LSMO film sensors studied, grown onto a STO [001] surface with a miscut angle [010] of 4°. (b) Schematics of WB-45° and WB-90° configurations. The orientation of the WB is fixed by the anisotropy axis of the LSMO thin film. (c) AMR and (d) MOKE hysteresis loops of a 30 nm thick LSMO film with the indicated WB configurations acquired at room temperature and with the field applied parallel to the hard axis. Note the great difference between the AMR hysteresis loops, originated from the independent direction of magnetization rotation which reduces the 45° WB AMR ratio, while the MOKE hysteresis confirms that it is the same sample. (e) Thickness-dependent saturation field (anisotropy field) derived from AMR and MOKE measurements. As expected, the anisotropy field increases slightly with the thickness. A linear fit to the data (gray line) shows an increase of the anisotropy field with a thickness of 0.016 mT/nm.

followed by ion beam etching in argon. Typically, the magnetoresistive sensors were patterned in a WB configuration (see Supporting Information) with four identical 100 μm wide and 500 μm long arms.

Before exposing the sensors to biological scenarios, the device was completed by encapsulation with a PDMS coating (Sylgard 184, Dow Corning) to electrically isolate the LSMO circuit from the physiological milieu. We chose PDMS as an isolating layer for its chemical stability and demonstrated long-term biocompatibility *in vivo*.[23−26] Generally, coatings of 100 μm were used. For *in vitro* tests, 50 μm coating proved to provide the same good isolating and endurance results. Although thicker than other reported passivation coatings,[17,18] PDMS provide a soft interface for a good mechanical compliance with the biological tissue[27] and can be patterned in a variety of ways to tune the tissue response.[28,29] In this work, the PDMS encapsulating film was patterned with a grating structure (10 × 5 × 20 μm, width x height x pitch) *via* soft lithography, which has been proved to guide the growth of axons bundles longitudinally aligned to the grating structures.[30]

Performance Characterization. We tested the magnetoresistive response of the sensors at different angles and temperatures. First, we

https://doi.org/10.1021/acsbiomaterials.2c01147
ACS Biomater. Sci. Eng. 2023, 9, 1020−1029

determined the most sensitive orientation of the sensor, that is, its hard axis. For this, we implemented a rotating sample holder between two fixed electromagnets. This allowed us to rotate the sensor 360° in 0.9° steps, while a 2 Hz sine field of 3.44 mT amplitude was applied. In this way, we scanned the dependence of the AMR on the applied field under different angles. MOKE magnetometry was performed in the patterned samples to independently determine the hard axis and anisotropy field of the sensors and compare them with the AMR results. In this case, a rotating magnetic field was produced by a two-axis electromagnet. The MOKE setup used a blue laser (450 nm wavelength) to maximize the Kerr rotation in LSMO.[31]

Next, we recorded the sensor response as a function of temperature in the range of interest for detecting biological magnetic signals (i.e., 37 °C up to 45 °C), by using a homemade setup which includes a heater below the sample holder and a temperature controller with an accuracy of 0.01 °C. The sensor was tested up to 45 °C to ensure a good operability sufficiently above 41 °C.

This sample holder was placed between two pairs of electromagnets which allowed us to accurately record the variation of the sensitivity with the magnetic field, at each temperature, by a modulation technique. Briefly, at each value of the applied constant magnetic field, we added a small sinusoidal field, δb = 8.6 μT, with a frequency of 2 Hz, and recorded the response to the latter to obtain the sensitivity at that applied field. This temperature setup allowed us to find the temperature at which each sensor presents its optimum sensitivity. In addition, we recorded the noise of the sensor as a function of voltage bias. For signal amplification, the first stage consisted of a custom-made amplifier with selected characteristics to match the output resistance range of the sensors (as it varies with thickness). The signal was again amplified by a commercial low-noise amplifier SR560, with a 0.01 Hz to 3 kHz filter. The overall gain of the system was 2.5 × 10^5 V/A. The signal was finally digitalized using a USB-6363 NI DAQ, and the data were analyzed using a custom-made MATLAB program.

***In Vitro* Biological Response Tests.** All the experiments were performed in accordance with the EU guidelines (2010/63/UE) and Italian law (Decree 26/14) and were approved by the local authority veterinary service and by our institution (SISSA) animal well-being committee (OBPA). Animal use was approved by the Italian Ministry of Health (no. 22DABNQYA), in agreement with the EU Recommendation 2007/526/CE. Organotypic cultures were obtained from the spinal cords of E12 embryonic mouse (C57BL) as previously reported.[32,33] We tested the biocompatibility of the PDMS-encapsulated LSMO when interfaced to the spinal explant growth by coculturing embryonic spinal cord and dorsal root ganglia (DRG) thin slices for 4 weeks *in vitro*. These organ slices represent a complex *in vitro* model where sensory-motor cytoarchitecture, synaptic properties, and spinal cord resident cells are retained in a 3D fashion.[33] By the use of this model, we have recently shown that artificial scaffolds enriched with nanostructures sustain axonal regeneration and spinal segment rewiring.[32] Such tests were predictive and instrumental for *in vivo* scaffold implantation.[34] Live calcium imaging was performed as previously reported;[35] briefly, organotypic spinal cords were loaded with cell permeable Ca^{2+} dye Fluo-4 AM (Molecular Probes); 11.6 μL of DMSO (Sigma-Aldrich) was added to the stock 50 μg of the dye; and cultures were incubated at 4 μM final concentration. After dye loading and de-esterification, cultures were maintained in extracellular saline solution of the following composition (mM): 150 NaCl, 4 KCl, 2 $CaCl_2$, 1 $MgCl_2$, 10 HEPES, 10 glucose (pH adjusted to 7.4 with NaOH; osmolarity 300 mOsm). Samples were mounted on an inverted microscope (Nikon Eclipse Ti−U). The dye was excited at 488 nm, and the emission was detected at 520 nm, and cultures were observed with a 40× objective (PlanFluor, 0.60 NA). Images were acquired every 150 ms using the ORCA-Flash4.0 V2 sCMOS camera (Hamamatsu) operating at binning 4. Drugs used: 25 μM bicuculline (GABAA receptor antagonist; Sigma-Aldrich, St Louis, Missouri, USA) and 2 μM strychnine (glycine receptor antagonist; Sigma-Aldrich) perfused for 20 min to weaken the synaptic inhibition and increase the synchronization. Finally, 1 μM TTX (a voltage-gated, fast Na^+ channel blocker; Latoxan, Portes-lès-Valence, France) was added to confirm the neuronal nature of the recorded signals. Images were analyzed with ImageJ software (NIH), and the corresponding traces were extracted with Clampfit software (pClamp suite, 10.4 version, Axon Instruments, San Jose, CA, USA). Following calcium imaging, organotypic slices were fixed in 4% formaldehyde, prepared from fresh paraformaldehyde, in PBS 1× for at least 1 h. After fixation, slices were incubated for 10 min with 0.1 m glycine in PBS 1× and permeabilized for 1 h with 0.3% Triton-X-100 (Carlo Erba, Emmendingen, Germany) in PBS 1× added with 5% FBS (Gibco) and 4% BSA (Sigma-Aldrich) to prevent nonspecific binding of primary antibodies. Samples were subsequently incubated with primary antibodies overnight at 4 °C and with the secondary antibodies for 2 h at room temperature.[35] Mounting was performed with antifade medium Fluoromount (Sigma-Aldrich) on 1 mm thick microscope glass slides. The samples were incubated with the anti-β-tubulin III primary antibody (1:800, Sigma-Aldrich) and visualized with Alexa 594 antirabbit in goat as the secondary antibody (1:800, Invitrogen) and with antineurofilament H (SMI-32, 1:800, Biolegend) recognized by Alexa 488 antimouse in goat as the secondary antibody (1:800, Invitrogen). Nuclei were stained with DAPI (1:500, Invitrogen). A Nikon Eclipse Ti2 inverted microscope connected to an A1R confocal system (Nikon Instruments) was used to acquire stitched images (10× Plan Apo λ, 0.45 NA) to obtain a morphological insight of the stained spinal cord slice cultures.

***In Vivo* Biological Response Tests.** Subcutaneous implantation studies were conducted in female Sprague Dawley rats in accordance with the German animal welfare law (approval number: G 17-15-040 by Landesuntersuchungsamt Rheinland-Pfalz). The animal experimental procedures used were approved by the responsible investigatory agency. The rats were housed in groups under standardized hygienic conditions in open cages type 4 with free access to food and water. For the implantation, rats were anesthetized by isoflurane inhalation. The analgesia of the animals was performed with subcutaneously injected meloxicam (1 mg/kg body weight) and daily administration thereafter for over 4 days. PDMS-encapsulated LSMO sensors were subcutaneously implanted for 7 days (subacute phase) and then over a period of 8 weeks (chronic phase) in rats at the age of 10 weeks (N = 5 per group). After implantation, the animals were monitored daily for body weight, changes in behavior, and wound healing. After 7 days or 8 weeks, rats were sacrificed by euthanasia with CO_2 inhalation. For the detection of major systemic toxicity signs, the weight of the total body and major inner organs (i.e., liver, lung, kidneys, and spleen) and hematological parameters (i.e., number of lymphocytes, neutrophils, eosinophils, basophils, and monocytes in peripheral blood) were determined. Blood samples for the blood smear were analyzed by the wedge technique. After air-drying, blood smears were stained with the Hemacolor rapid staining kit (Sigma-Aldrich). This test uses the Pappenheim staining for the differentiation of single immune cells. Histological examination of the skin at the implantation sites was carried out by Hematoxylin & Eosin (HE) staining and Masson's Trichrome (MTC) staining. A piece of skin surrounding the implantation site was cut out and fixed in 4% formalin. After dehydration by means of an ascending alcohol series and embedding in paraffin, skin slices (4 μm) were prepared and stained with HE staining (Morphisto) and MTC staining (Engelbrecht Medizin-und Labortechnik).

RESULTS AND DISCUSSION

Sensor Performance Characterization. The LSMO WB of Figure 1a fabricated as described in the previous section were tested with two different configurations, in the following named as WB-45° and WB-90°, as shown in Figure 1b. The output voltage of the sensors is always measured between the S + and S− electrodes depicted in the figure. The orientation of the WB is given by the alignment of the arms respect to the anisotropy axis of the LSMO thin film. In the WB-90° configuration, two arms of the bridge are aligned with the easy

https://doi.org/10.1021/acsbiomaterials.2c01147
ACS Biomater. Sci. Eng. 2023, 9, 1020−1029

axis (energetically favorable direction of the spontaneous magnetization) and the other two with the hard axis (perpendicular to the easy one), whereas in the case of the 45° configuration, the sensor is rotated 45° respect to the WB-90°. The latter configuration allows us to obtain a linear response at zero field without the need of an extra deposition of a metal over LSMO.[36] In the particular case of WB-90°, a magnetic field bias was added to get a linear response around the bias field.

We first analyze the output voltage (between the S+ and S− electrodes) dependence of the two different WB configurations (WB-45° and WB-90°) with the applied magnetic field aligned parallel to the hard axis of the LSMO thin film, as indicated in Figure 1a,b. The AMR response, this is the ratio between the resistance at an applied magnetic field (H) and that at the anisotropy field H_k (field at which the resistance saturates), is very different in both configurations, as shown in Figure 1c. This originates from the different AMR terms of the resistivity tensor that are involved in WB-90° and WB-45° bridges. Similar observations have been carried out for different LSMO thicknesses. The two configurations display distinctive AMR curves, whereas similar magnetic responses, with a slightly larger H_k values as the thickness increases, as Figure 1e shows.

For WB-90°, the response corresponds to the transversal component of magnetization; thus, we inferred that the hard axis angle is the orientation at which the AMR response is maximum. However, for the WB-45° configuration, the maximum response is achieved when the magnetization forms 45° with the easy axis and linear AMR around zero applied field is expected. Besides, due to clock and anticlockwise rotation of the magnetization, the output at the hard axis is very small, that is, the magnetization could rotate in both senses as they are equally energetically favorable. Therefore, in such a configuration, we determined the hard axis as the orientation where the output signal is nearly zero as a function of the external field, and once oriented, the saturation field was obtained as the saturation field at an angle 0.9° off the hard axis (experimental setup described in the Materials and Methods section). In that situation, the small component along the easy axis was enough to give a preferential direction for the magnetization rotation. The butterfly-like behavior observed in Figure 1c is due to such small easy axis field component at the WB-45° configuration when the AMR changes its sign. In both cases, the hard axis direction was at 90° to the direction of the step edges of the vicinal substrates, as expected, and the saturation field was determined as the field where the AMR becomes constant with the external field.

The anisotropy field was determined as well by means of vectorial MOKE magnetometry. In this case, the position of the sensor hard axis was determined as the orientation where the transverse component of the magnetization changes its sign. Figure 1d depicts examples of the magnetization (M) vs. H hysteresis loops close to the hard axis. By using the data obtained on these experiments, we estimated H_k as the saturation field of the longitudinal component at the hard axis. The dependence of H_k on the LSMO thickness in the longitudinal component is depicted in Figure 1e, together with those obtained from AMR experiments.

We observe that the evolution of the saturation field with thickness is the same for both AMR and MOKE characterizations, as expected. The anisotropy field slightly increases with the thickness, in agreement with the previous results.[37] The configuration (45°/90°) of the sensors does not affect the anisotropy field, thus indicating that the shape anisotropy does not play a key role in the magnetization dynamics of the sensors. This behavior is expected, given the low saturation magnetization of the LSMO films at room temperature. This is an advantage over the commonly used permalloy sensors, as it gives us more flexibility in terms of geometry design.

After having determined the hard axis orientation, thus the measuring orientation, we measured the maximum value of the normalized sensitivity (mathematical expression in the Supporting Information), and the AMR for every sensor at temperatures amid human body values (from 37 to 41 °C, see the Materials and Methods section). The resulting averaged values are shown in Figure 2 as a function of the LSMO

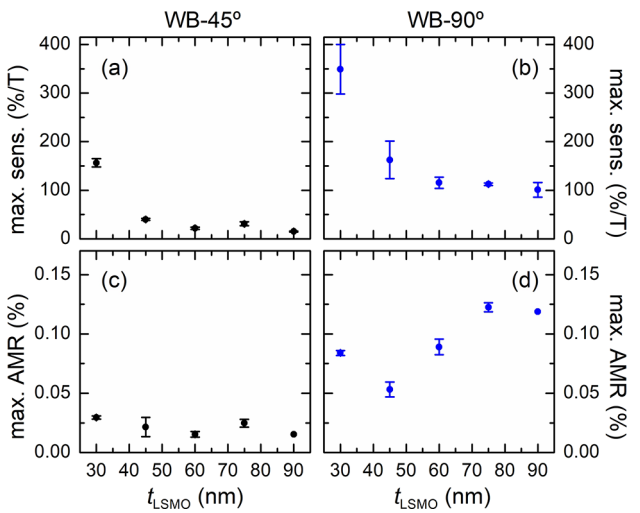

Figure 2. Thickness-dependent sensor characterization using (a,c) WB-45° and (b,d) WB-90° configurations. Both sensitivity (top) and AMR (bottom) values are derived from magneto-transport measurements performed at the best temperature performance of the sensor.

thickness for both WB configurations (averages over two to four different sensors for each thickness; error bars represent the standard error of the mean). We observed that the sensitivity of the sensors is not correlated with their maximum AMR.

Indeed, both anisotropy field and AMR affect the sensitivity of the sensor.[21] Among the studied sensors, we obtained a maximum sensitivity of 400%/T for the 30 nm thick sensor configured as WB-90° (see Figure 2b). In the following, we performed an in-depth characterization of this sensor, which was the one with the highest sensitivity.

Figure 3a,b depicts, respectively, the evolution of the maximum sensitivity and AMR of the selected sensor with temperature. The sensitivity of the sensor presents a peak of almost 400%/T at 41 °C, which is therefore its optimum performance temperature and is above 300%/T between 37.5 and 42.5 °C. Figure 3c, d shows, respectively, examples of the sensitivity and AMR vs. H curves at that temperature. The indent in the sensitivity curves is due to the change of sign of the derivative of V_{out} with respect to H close to zero applied field (see the used modulation technique explanation in the Materials and Methods section and eq S1 in the Supporting Information). The peak in the maximum sensitivity with temperature (Figure 3a) is not reproduced in the evolution of the AMR (Figure 3b) because the anisotropy field varies with

https://doi.org/10.1021/acsbiomaterials.2c01147
ACS Biomater. Sci. Eng. 2023, 9, 1020−1029

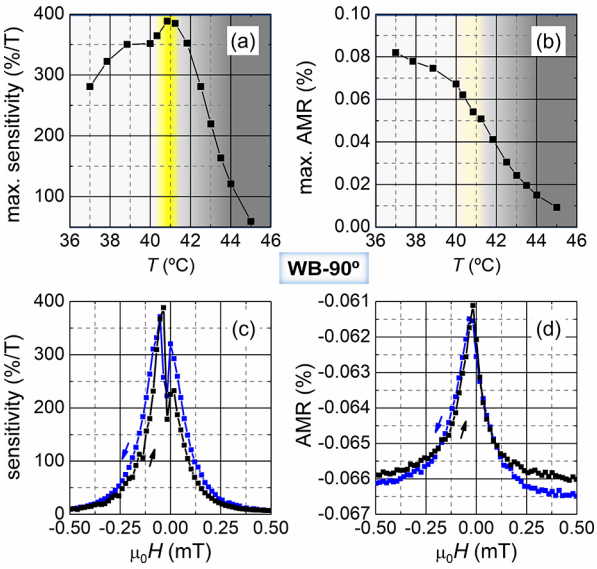

Figure 3. Searching the best temperature sensor performance. (a,b) Variation of the maximum sensitivity and AMR with temperature, respectively, for a WB-90° and 30 nm thick sensor. Note that both maximum sensitivity and AMR vanish approaching T_c (dark shadowed area) and that the temperature of maximum sensitivity is 41 °C (yellow), at which the maximum AMR still shows a relevant value. (c,d) Examples of the variation of the sensitivity and AMR (in absolute value), respectively, of the sensor with the applied magnetic field along the hard axis for 41 °C. Black (blue) points correspond to the values obtained when going from negative (positive) to positive (negative) H values as indicated by the arrows. Values in (a,b) are extracted from curves as those in (c,d).

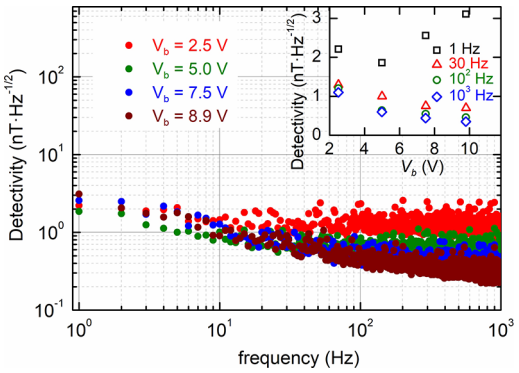

Figure 4. Sensor detectivity performance as a function of frequency at different V_b for a 30 nm thick WB-90° LSMO sensor (at 41 °C). The results are comparable to those of commercial sensor HMC1001 also shown in the figure (V_b = 5.5 V), which is engineered with flux concentrators, unlike the simple LSMO sensors presented here. Inset: evolution of the detectivity as a function of V_b for frequencies of 1, 10, 100, and 1000 Hz. Notice that the detectivity does not improve with V_b at low frequencies (where the $1/f$ dominates), whereas at higher frequencies where the thermal noise dominates, the detectivity can be reduced increasing V_b. Remarkably, the detectivity value is 2−3 nT·Hz$^{-1/2}$ at low frequency (1 Hz), 1 nT·Hz$^{-1/2}$ at 10 Hz and reaching 0.3 nT·Hz$^{-1/2}$ at 100 Hz.

temperature as well, *i.e.,* as the material is heated and approaches T_c, its anisotropy field is reduced.

Finally, we measured the detectivity at different bias voltages in the selected sensor of maximum sensitivity at its optimum working temperature. This magnitude is given by the ratio between the power spectral density (PSD) and the sensitivity (mathematical expressions given in eqs S1−S3 in the Supporting Information) and represents the minimum detectable magnetic field at a given frequency (see details of the experimental configuration in the Materials and Methods section). The results are shown in Figure 4.

The PSD values obtained at different bias voltages (see Figure S1 in Supporting Information) prove that indeed these devices have an extremely low $1/f$ noise component at low bias voltages (V_b < 5 V). In this regime, the electronic noise is dominated by the thermal noise of the sensor. When increasing the bias voltage above 5 V, this $1/f$ component starts to predominate in the low-frequency range. At these frequencies, the detectivity does not improve by increasing the bias voltage because both the PSD and sensitivity are proportional to V_b. However, for higher frequencies (above the $1/f$ knee), the noise is dominated by the thermal component and therefore can still be improved increasing the bias voltage (see inset in Figure 4). Regarding the behavior at low frequencies, we obtain a detectivity as low as < 2 nT·Hz$^{-1/2}$ at 1 Hz in the optimum conditions of the sensor.

This measured detectivity of the sensor is close to one of the commercial AMR sensors like the HMC10xx series that typically yields 0.2 nT·Hz$^{-1/2}$ at 1 Hz (value extracted from its datasheet information). Importantly, the results for our sensor were obtained without the use of flux concentrators, which are included in the commercial HMC10xx series. These flux concentrators are known to decrease the detectivity by one order of magnitude or more[38−40] and would be an additional improvement to the LSMO sensors presented here. The obtained detectivities can be compared as well with those of other GMR sensors, which have been already used in the detection of biomagnetic signals.[17] The sensors described in those experiments exhibited low-frequency detectivities of ∼3 nT·Hz$^{-1/2}$ at 1 Hz, very similar to those of our LSMO sensors, whereas their sensing area was significantly larger (400 μm × 1.7 mm). Hall sensors display very low noise levels and have been proposed for biomedical applications as well.[41] However, their sensitivity is typically worse than that of AMR sensors and their lowest reported nominal detectivity without flux concentrators remains at 20 nT·Hz$^{-1/2}$.[42] Commercial MR sensors have similar values of detectivity to our sensors.[10] However, it is important to note that the vast majority of them have magnetic flux concentrators implemented on-chip, which, as mentioned above, can increase significantly the effective sensitivity of the device. In our case, the sensors do not need such a device to present a similar detectivity, thus we could expect to obtain even lower detectivity values if similar flux concentrators are used.

Biocompatibility Studies. In order to explore the potential of the newly developed LSMO sensors as implantable biomagnetic detectors, we carried out *in vitro* and *in vivo* biocompatibility tests on a series of sensors encapsulated by a PDMS coating directly over the LSMO WB, as explained in the Materials and Methods section (Figure 5a). This polymeric layer acts as an electric insulator of the LSMO circuit, which needs to be preserved from the physiological milieu and provides a soft biocompatible surface to interfacing the biological tissue (see Materials and Methods section).

The PDMS encapsulating film was further patterned with a grating structure to stabilize the spinal/LSMO interface and to promote the directionality of the axons bundles with respect to the sensor components. A control over axons geometry might

https://doi.org/10.1021/acsbiomaterials.2c01147
ACS Biomater. Sci. Eng. 2023, 9, 1020−1029

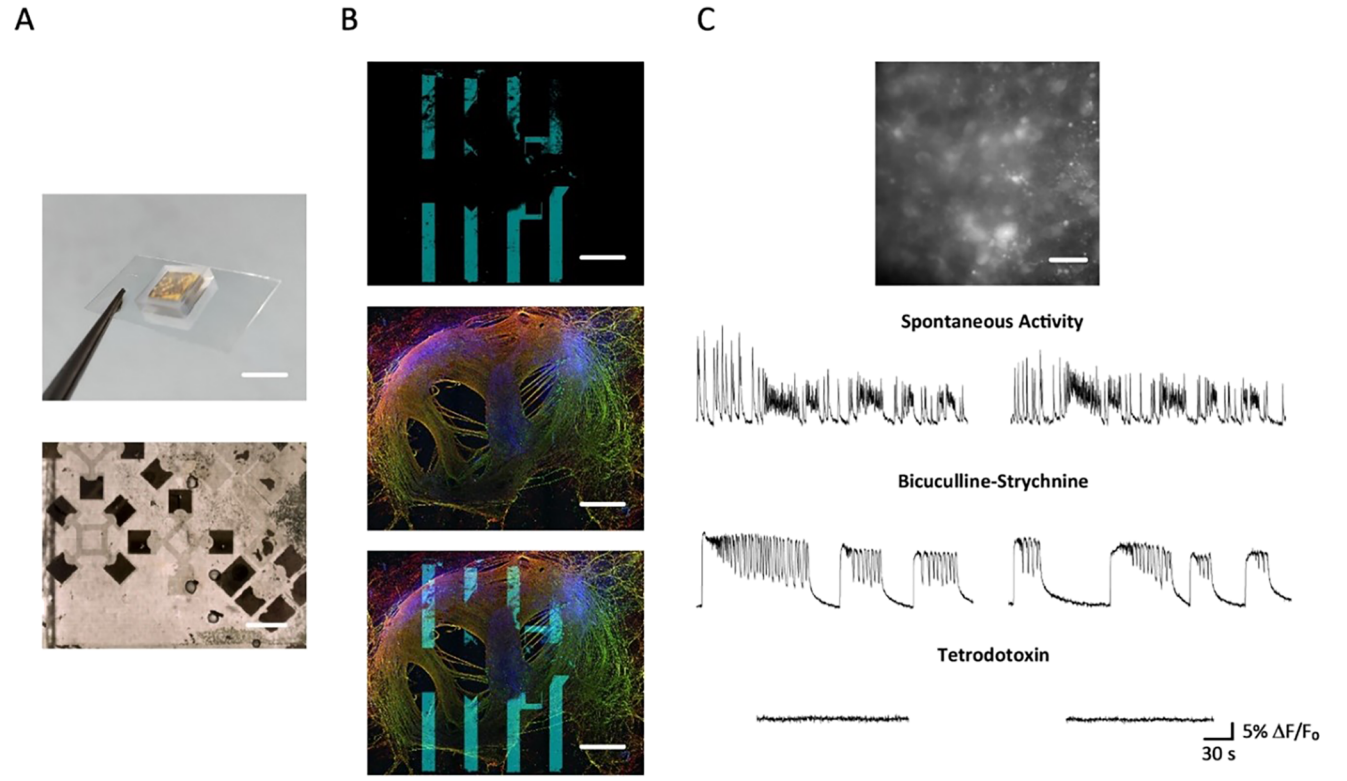

Figure 5. *In vitro* biocompatibility tests of PDMS-coated LSMO sensors with 1-month organotypic spinal cultures. (a) Top, the full PDMS wafer containing the LSMO sensor is shown. Scale bar = 8 mm. The substrate was pasted on top of a glass coverslip to facilitate its handling and culturing. Bottom, a bright-field top view image of the sensor circuitry embedded in the PDMS is also provided. Scale bar = 500 μm. (b) Representative confocal reconstructions show, respectively, a portion of LSMO sensor circuitry to which the spinal cord slice was interfaced (top); the entire organotypic slice (middle) stained with anti-β-tubulin III (red) and SMI-32 anti-neurofilament-H (green) and DAPI (blue); merged image (bottom). Scale bars = 800 μm. (c) Top inset, snapshot at 40× magnification of a spinal cord culture loaded with Fluo4-AM. Scale bar = 50 μm. Two representative traces of calcium transients are shown depicting basal spontaneous activity (top) and bicuculline-strychnine activity (middle) and TTX effects (bottom). Calcium transients are expressed as fractional amplitude increase ($\Delta F/F0$).

favor future detection of voltage signals due to action potentials firing.

The ultimate potential of our novel LSMO sensor for biomedical applications resides in its integration with the neuronal tissue *in vitro* and its stability and tissue reactivity upon exposure to the biological milieu *in vivo*. Biocompatibility tests *in vitro* were carried out by interfacing PDMS-encapsulated LSMO prototypes to spinal cord tissue explants maintained in culture for weeks.[32] Specifically, we monitored the organotypic spinal segments development and the emergence of synaptic activity in a controlled microenvironment integrated to LSMO sensors for 1 month. The long-term stability of spinal tissue interfaced to the sensor is depicted in Figure 5b, which shows confocal reconstructions of LSMO-spinal slices. These low-magnification images enable the visualization of the entire area of tissue growth, characterized by the spinal slice, at the center, and the surrounding area where DRG and a huge network of outgrowing fibers form a typical regenerative belt of axons.[43] A distinct feature of healthy organotypic spinal slices is their ability to display prominent spontaneous electrical activity. We monitored the neuronal activity of the tissue *via* fluorescent live calcium imaging[35] (see details in the Materials and Methods section). In Figure 5c (top tracings), calcium episodes emerging as irregular events are shown, reflecting spontaneous synaptic activity, typical of these preparations, without single-action potentials or individual postsynaptic current resolution. The presence of such episodes of activity in LSMO-slices is a recognized measure of the network healthy state. To examine the functional consequences of LSMO long-term interfacing on spinal network dynamics, we used strychnine (2 μM) and bicuculline (25 μM) (i.e., glycine/γ-aminobutyric acid type A—$GABA_A$—receptor antagonists) to weaken synaptic inhibition. In LSMO slices, as previously reported,[43] the pharmacological block of spinal inhibition turns network dynamics from random events to synchrony, leading to the emergence of slow-paced and regular bursting (Figure 5c, middle tracings). The neuronal and synaptic nature of the detected calcium events are supported by experiments, where tetrodotoxin (TTX 1 μm; a blocker of voltage-gated, fast Na^+ channels) blocks all calcium activity (Figure 5c, bottom tracings). The described organotypic slice functional features are strong indicators of the healthy development of spinal networks once integrated and upon long-term exposure to LSMO sensors.

Equivalent PDMS-encapsulated LSMO sensors over STO substrates shaped into disks of 5 mm in diameter (Figure 6a) were subcutaneously implanted for 7 days (subacute phase) and then over a period of 8 weeks (chronic phase) in female Sprague Dawley rats at the age of 10 weeks (see the Materials and Methods section). The coated sensors were implanted in a skin pocket practiced at the back of the rat. A second pocket served as the control, thus receiving PDMS disks of the same size but without sensors (*ca.* 8 mm in diameter and 700 μm in

https://doi.org/10.1021/acsbiomaterials.2c01147
ACS Biomater. Sci. Eng. 2023, 9, 1020−1029

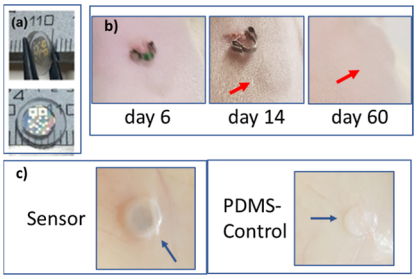

Figure 6. *In vivo* biocompatibility tests of PDMS-encapsulated LSMO sensors in subcutaneous pockets in a rat model. (a) Lateral and top view of a LSMO encapsulated sensor before implantation. (b) Gross view of the wound healing process at the site of implantation at different time points. The red arrows indicate the location of the sensor under the skin. (c) Representative images of the sensor and the PDMS control at the explantation time (8 weeks). Blue arrows point the implant encapsulated in the subcutaneous connective tissue.

thickness). After the careful positioning of the implant, the skin pockets were closed with suture clips.

The sensor implantation did not induce remarkable changes on the normal growth development of the rats at either the subacute or the chronic time points in any of the conditions tested. Moreover, the animals showed normal behavior regarding intake of food and water, as well as grooming activities. At the implantation site, the wound healing process showed no sign of inflammation, rejection reaction against the implant, or hypergenesis. A gross inspection of the implantation sites revealed the formation of a normal scar without visible signs of inflammation in all cases (Figure 6b). Importantly, none of the treated rats showed pain or defense reactions during palpation on the movable implants. Systemically, no abnormalities could be determined in any of the internal organs investigated (i.e., liver, kidneys, spleen, lungs) neither at their weight nor at the histological level (Figure S2). Clinical evidence such as extension, swelling, or plaque were not found in any of the viscera examined. The amount of lymphocytes, neutrophils, eosinophils, basophils, and monocytes in peripheral blood showed no aberrance compared to reference values, neither in the subacute nor in the chronic phase studies.

Closer inspection of the skin at the implantation site showed a thin layer of connective tissue surrounding the implant in all cases (Figures 6c and S3). The skin around the implanted materials showed no signs of inflammation or pathological changes. No redness, swelling, or any hardening could be observed. The process of lesion healing and regeneration was found comparable to that in control implantation sites and within the range of a normal wound healing process, with sporadic immune cells and a slight fibrous tissue encapsulation of connective tissue induced by the presence of the implant (Figures 6c and S3).

For a further inspection of the local tissue response to the implantation of the LSMO sensors, histological examination of the skin at the implantation sites was carried out by HE and MTC stainings (see the Materials and Methods section). Results showed that a thin connective tissue capsule was formed in both the PDMS-coated LSMO sensors and the PDMS control (Figure S3), surrounding the cavity in which the implant was located, without an evident foreign body reaction against the sensor material. All together, these findings indicate a biocompatible response of the skin tissue to the implantation of these LSMO sensors.

After explantation, the sensors were visually and electrically examined. No appreciable damage either in the sensor or the PDMS coating was observed after 8 weeks of implantation (see images in Figure S4). In order to check the electrical resistance of the sensors and so verify their electrical status, they were first decapsulated from the PDMS coating and then wire bonded through their gold pads. During this decapsulation process, the gold pads, which got fixed to the PDMS coating layer, got damaged. Although this implied a higher recorded resistance for these sensors with respect to their original state, they were fully operative after explantation and decapsulation.

A final on-bench test was performed to verify the stability of the PDMS-encapsulated sensor in working conditions, when the temperature could rise locally in some parts of the circuit. For this, we used one of the sensors that had been implanted and decapsulated and prepared a full prototype with electric connections to the WB bridges, which was again fully encapsulated in PDMS (see Figure S5). This PDMS-coated prototype was permanently biased with a 10 V voltage and tested each 30 min, for 7 days, while it was externally and continuously heated at 37 °C, plus another subsequent 7 days heating at 45 °C. As the overall magnetic properties of LSMO are strictly correlated to the composition, a very tiny change in the oxygen content may affect drastically the magnetic phase of LSMO and hence its resistance. For this sensor, the resistance was 2.79 ± 0.042 kΩ before subcutaneous implantation and stayed at 2.82 ± 0.036 kΩ after all subsequent tests, with no significant variation. In addition, neither deterioration nor delamination of its respective PDMS coating was observed during this 14-day period.

CONCLUSIONS

We have demonstrated that LSMO-based AMR sensors can reach sufficiently low detectivity to be used for the detection of biomagnetic signals such as those produced by neural tissues. Specifically, we have studied two WB configurations regarding the orientation of the current respect to the material magnetization, WB-45° and WB-90°. For linearizing their response at zero field, we have used the 45° one. The best performance is achieved for 30 nm thick WB-90° devices with a detectivity <2 $nT \cdot Hz^{-1/2}$ at 1 Hz, which represents a comparable performance than that of GMR magnetic sensors. In addition, AMR technology presents advantages for industrial implementation because it employs single-layer systems. We have recorded significantly a low-noise level for our LSMO-based magnetic sensors, which is an intrinsic property of the material due to its crystalline quality. Since the best performance of these sensors is given at the LSMO metal−insulator transition that is close to the body temperature range, the use of these devices for sensing low-frequency biomagnetic signals is highly promising. This potential is further supported by the biocompatible responses obtained with our sensors both *in vitro* with organotypic spinal slices and *in vivo* in subcutaneous pockets in rats for up to two months of implantation.

ASSOCIATED CONTENT

Supporting Information

The Supporting Information is available free of charge at https://pubs.acs.org/doi/10.1021/acsbiomaterials.2c01147.

https://doi.org/10.1021/acsbiomaterials.2c01147
ACS Biomater. Sci. Eng. 2023, 9, 1020−1029

Definition of characterization magnitudes, description of the Wheatstone Bridge output, and supplementary figures of the PSD of the sensors and of the *in vivo* sensor characterization (PDF)

AUTHOR INFORMATION

Corresponding Author

María Teresa González − *Fundación IMDEA Nanociencia, Madrid 28049, Spain;* orcid.org/0000-0002-7253-797X; Email: teresa.gonzalez@imdea.org

Authors

Arturo Vera − *Fundación IMDEA Nanociencia, Madrid 28049, Spain*

Isidoro Martínez − *Fundación IMDEA Nanociencia, Madrid 28049, Spain; Faculty of Experimental Sciences, Universidad Francisco de Vitoria, Pozuelo de Alarcón, Madrid 28223, Spain*

Luiz Guilherme Enger − *Normandie University, UNICAEN, ENSICAEN, CNRS, GREYC, Caen 14000, France;* orcid.org/0000-0002-6023-1439

Bruno Guillet − *Normandie University, UNICAEN, ENSICAEN, CNRS, GREYC, Caen 14000, France;* orcid.org/0000-0003-4091-0247

Rubén Guerrero − *Fundación IMDEA Nanociencia, Madrid 28049, Spain*

José Manuel Diez − *Fundación IMDEA Nanociencia, Madrid 28049, Spain; Departamento Física de la Materia Condensada, Universidad Autónoma de Madrid, Madrid 28049, Spain*

Olivier Rousseau − *Normandie University, UNICAEN, ENSICAEN, CNRS, GREYC, Caen 14000, France;* orcid.org/0000-0003-2739-1710

Marc Lam Chok Sing − *Normandie University, UNICAEN, ENSICAEN, CNRS, GREYC, Caen 14000, France*

Victor Pierron − *Normandie University, UNICAEN, ENSICAEN, CNRS, GREYC, Caen 14000, France*

Paolo Perna − *Fundación IMDEA Nanociencia, Madrid 28049, Spain;* orcid.org/0000-0001-8537-4834

Jaime J. Hernández − *Fundación IMDEA Nanociencia, Madrid 28049, Spain;* orcid.org/0000-0002-4368-2529

Isabel Rodríguez − *Fundación IMDEA Nanociencia, Madrid 28049, Spain;* orcid.org/0000-0002-7178-8275

Ivo Calaresu − *International School for Advanced Studies (SISSA/ISAS), Trieste 34136, Italy*

Anja Meier − *mfd-Diagnostics GmbH, Wendelsheim 55234, Germany*

Carmen Huck − *mfd-Diagnostics GmbH, Wendelsheim 55234, Germany*

Ana Domínguez-Bajo − *Instituto de Ciencia de Materiales de Madrid (ICMM), CSIC, Madrid 28049, Spain;* Present Address: UCLouvain, Louvain Institute of Biomolecular Science and Technology (LIBST), Animal Molecular and Cellular Biology group, Place Croix du Sud 5, 1348 Louvain la Neuve, Belgium; orcid.org/0000-0002-0835-7181

Ankor González-Mayorga − *Hospital Nacional de Parapléjicos, SESCAM, Toledo 45071, Spain*

Elisa López-Dolado − *Hospital Nacional de Parapléjicos, SESCAM, Toledo 45071, Spain; Research Unit of "Design and Development of Biomaterials for Neural Regeneration", Hospital Nacional de Parapléjicos, Joint Research Unit with CSIC, Toledo 45071, Spain*

María C. Serrano − *Instituto de Ciencia de Materiales de Madrid (ICMM), CSIC, Madrid 28049, Spain;* orcid.org/0000-0002-5010-644X

Laura Ballerini − *International School for Advanced Studies (SISSA/ISAS), Trieste 34136, Italy;* orcid.org/0000-0001-8420-0787

Lucas Pérez − *Fundación IMDEA Nanociencia, Madrid 28049, Spain; Dept. Física de Materiales, Universidad Complutense, Madrid 28040, Spain;* orcid.org/0000-0001-9470-7987

Rodolfo Miranda − *Fundación IMDEA Nanociencia, Madrid 28049, Spain; Departamento Física de la Materia Condensada and Instituto "Nicolás Cabrera" and Condensed Matter Physics Center (IFIMAC), Universidad Autónoma de Madrid, Madrid 28049, Spain*

Stéphane Flament − *Normandie University, UNICAEN, ENSICAEN, CNRS, GREYC, Caen 14000, France;* orcid.org/0000-0002-3337-512X

Laurence Méchin − *Normandie University, UNICAEN, ENSICAEN, CNRS, GREYC, Caen 14000, France;* orcid.org/0000-0002-6350-1801

Julio Camarero − *Fundación IMDEA Nanociencia, Madrid 28049, Spain; Departamento Física de la Materia Condensada and Instituto "Nicolás Cabrera" and Condensed Matter Physics Center (IFIMAC), Universidad Autónoma de Madrid, Madrid 28049, Spain;* orcid.org/0000-0003-0078-7280

Complete contact information is available at: https://pubs.acs.org/10.1021/acsbiomaterials.2c01147

Notes

The authors declare no competing financial interest.

ACKNOWLEDGMENTS

This work was funded by the European Union's Horizon 2020 research and innovation programme under grant agreement no. 737116. It was also partially funded by the Spanish MICINN projects BiSURE (DPI2017-90058-R), REGINNA (PID2020-120202RB-I00), MatMagSwitch (PID2020-117024GB-C43), ECLIPSE-ECoSOx (PID2021-122980OB-C52), FUN-SOC (RTI2018-097895-B-C42) and the "Severo Ochoa" Programme for Centres of Excellence in R&D (SEV-2016-0686), as well as by the Comunidad de Madrid though the project NanoMagCOST (CM S2018/NMT-4321).

REFERENCES

(1) Dagotto, E. Open questions in CMR manganites, relevance of clustered states and analogies with other compounds including the cuprates. *New J. Phys.* **2005**, *7*, 67.

(2) Han, S. J.; Xu, L.; Yu, H.; Wilson, R. J.; White, R. L.; Pourmand, N.; Wang, S. X. CMOS Integrated DNA Microarray Based on GMR Sensors *International Electron Device Meeting* San Francisco, CA, USA, **2006**, pp. 1-4, DOI: 10.1109/IEDM.2006.346887.

(3) Mao, S.; ChenLiu, Y. F.; Chen, X.; Xu, B.; Lu, P.; Patwari, M.; Xi, H.; Chang, C.; Miller, B.; Menard, D.; Pant, B.; Loven, J.; Duxstad, K.; Li, S.; Zhang, Z.; Johnston, A.; Lamberton, R.; Gubbins, M.; McLaughlin, T.; Gadbois, J.; Ding, J.; Cross, B.; Xue, S.; Ryan, P. *IEEE Trans. Magn.* **2006**, *42*, 97−102.

(4) Siwach, P. W.; Singh, H. K.; Srivastava, O. N. Low field magnetotransport in manganites. *J. Phys.: Condens. Matter* **2008**, *20*, 273201.

(5) Stutzke, N. A.; Russek, S. E.; Pappas, D. P.; Tondra, M. Low-frequency noise measurements on commercial magnetoresistive magnetic field sensors. *J. Appl. Phys.* **2005**, *97*, 10Q107.

(6) Wang, X.; Chen, Y.; Xi, H.; Dimitrov, D. V. *IEEE Electron Device Lett.* **2009**, *30*, 294−297.
(7) Zheng, C.; Zhu, K.; Cardoso de Freitas, S.; Chang, J.-Y.; Davies, J. E.; Eames, P.; Freitas, P. P.; Zakazova, O.; Kim, C.; Leung, C. W.; Liou, S.-H.; Ognev, A.; Piramanayagam, S. N.; Ripka, P.; Samardak, A.; Shin, K. H.; Tong, S.-Y.; Tung, M.-J.; Wang, S.-X.; Xue, S.; Yin, Z.; Pong, P. W. T. *IEEE Trans. Magn.* **2019**, *55*, 0800130.
(8) Guerrero, R.; Pannetier-Lecoeur, M.; Fermon, C.; Cardoso, S.; Ferreira, R.; Freitas, P. P. Low frequency noise in arrays of magnetic tunnel junctions connected in series and parallel. *J. Appl. Phys.* **2009**, *105*, 113922.
(9) Kurij, G.; Solignac, A.; Maroutian, T.; Agnus, G.; Guerrero, R.; Calvet, L. E.; Pannetier-Lecoeur, M.; Lecoeur, P. Low noise all-oxide magnetic tunnel junctions based on a La0.7Sr0.3MnO3/Nb:SrTiO3interface. *Appl. Phys. Lett.* **2017**, *110*, 082405.
(10) Deak, J. G.; Zhou, Z.; Shen, W. Tunneling magnetoresistance sensor with pT level 1/f magnetic noise. *AIP Adv.* **2017**, *7*, 056676.
(11) Quynh, L. K.; Tu, B. D.; Thuy, N. T.; Viet, D. Q.; Duc, N. H.; Phung, A. T.; Giang, D. T. Meander anisotropic magnetoresistance bridge geomagnetic sensors. *J. Sci.: Adv. Mater. Devices* **2019**, *4*, 327−332.
(12) Rousseau, O.; Flament, S.; Guillet, B.; Lam Chok Sing, M.; Méchin, L. *Proceedings* **2017**, *1*, 635.
(13) Wang, Z.; Wang, X.; Li, M.; Gao, Y.; Hu, Z.; Nan, T.; Liang, X.; Chen, H.; Yang, J.; Cash, S.; Sun, N. X. Highly Sensitive Flexible Magnetic Sensor Based on Anisotropic Magnetoresistance Effect. *Adv. Mater.* **2016**, *28*, 9370−9377.
(14) Boto, E.; Holmes, N.; Leggett, J.; Roberts, G.; Shah, V.; Meyer, S. S.; Muñoz, L.; Mullinger, K. J.; Tierney, T. M.; Bestmann, S.; Barnes, G. R.; Bowtell, R.; Brookes, M. J. Moving magnetoencephalography towards real-world applications with a wearable system. *Nature* **2018**, *555*, 657.
(15) Sumiya, S.; Kawabata, S.; Hoshino, Y.; Adachi, Y.; Sekihara, K.; Tomizawa, S.; Tomori, M.; Ishii, S.; Sakaki, K.; Ukegawa, D.; Ushio, S.; Watanabe, T.; Okawa, A. Magnetospinography visualizes electrophysiological activity in the cervical spinal cord. *Sci. Rep.* **2017**, *7*, 2192.
(16) Johnson, C. N.; Schwindt, P. D. D.; Weisend, M. Multi-sensor magnetoencephalography with atomic magnetometers. *Phys. Med. Biol.* **2013**, *58*, 6065−6077.
(17) Barbieri, F.; Trauchessec, V.; Caruso, L.; Trejo-Rosillo, J.; Telenczuk, B.; Paul, E.; Bal, T.; Destexhe, A.; Fermon, C.; Pannetier-Lecoeur, M.; Ouanounou, G. Local recording of biological magnetic fields using Giant Magneto Resistance-based micro-probes. *Sci. Rep.* **2016**, *6*, 39330.
(18) Caruso, L.; Wunderle, T.; Lewis, C. M.; Valadeiro, J.; Trauchessec, V.; Trejo Rosillo, J.; Amaral, J. P.; Ni, J.; Jendritza, P.; Fermon, C.; Cardoso, S.; Freitas, P. P.; Fries, P.; Pannetier-Lecoeur, M. *Neuron* **2017**, *13*, 1283−1291.
(19) Enger, L. G.; Flament, S.; Bhatti, I.-M.; Guillet, B.; Chok Sing, M. L.; Pierron, V.; Lebargy, S.; Diez, J. M.; Vera, A.; Martinez, I.; Guerrero, R.; Perez, L.; Perna, P.; Camarero, J.; Miranda, R.; Gonzalez, M. T.; Méchin, L. *IEEE Trans. Magn.* **2022**, *58*, 4001204.
(20) Méchin, L.; Wu, S.; Guillet, B.; Perna, P.; Fur, C.; Lebargy, S.; Adamo, C.; Schlom, D. G.; Routoure, J.-M. Experimental evidence of correlation between 1/fnoise level and metal-to-insulator transition temperature in epitaxial La0.7Sr0.3MnO3thin films. *J. Phys. D Appl. Phys.* **2013**, *46*, 202001.
(21) Perna, P.; Rodrigo, C.; Jiménez, E.; Mikuszeit, N.; Teran, L.; Méchin, J.; Camarero, R.; Miranda, F. J. Magnetization reversal in half metallic La0.7Sr0.3MnO3 films grown onto vicinal surfaces. *J. Appl. Phys.* **2011**, *109*, 07B107.
(22) Perna, P.; Maccariello, D.; Ajejas, F.; Guerrero, R.; Méchin, L.; Flament, S.; Santamaria, J.; Miranda, R.; Camarero, J. Engineering Large Anisotropic Magnetoresistance in La0.7 Sr0.3 MnO3 Films at Room Temperature. *Adv. Funct. Mater.* **2017**, *27*, 1700664.
(23) Güven, D.; Weiland, J. D.; Maghribi, M.; Davidson, J. C.; Mahadevappa, M.; Roizenblatt, R.; Qiu, G.; Krulevitz, P.; Wang, X.; LaBree, L.; Humayun, M. S. Implantation of an inactive epiretinal poly(dimethyl siloxane) electrode array in dogs. *Exp. Eye Res.* **2006**, *82*, 81−90.
(24) Heo, C.; Park, H.; Kim, Y.-T.; Baeg, E.; Kim, Y. H.; Kim, S.-G.; Suh, M. A soft, transparent, freely accessible cranial window for chronic imaging and electrophysiology. *Sci. Rep.* **2016**, *6*, 27818.
(25) Li, J.; Kang, L.; Yu, Y.; Long, Y.; Jeffery, J. J.; Cai, W. X.; Wang, X. Study of long-term biocompatibility and bio-safety of implantable nanogenerators. *Nano Energy* **2018**, *51*, 728−735.
(26) Tohfafarosh, M.; Sevit, A.; Patel, J.; Kiel, J. W.; Greenspon, A.; Prutkin, J. M.; Kurtz, S. M. Characterization of Outer Insulation in Long-Term-Implanted Leads. *J. Long Term Eff. Med. Implants* **2016**, *26*, 225−232.
(27) Brown, X. Q.; Ookawa, K.; Wong, J. Y. Evaluation of polydimethylsiloxane scaffolds with physiologically-relevant elastic moduli: interplay of substrate mechanics and surface chemistry effects on vascular smooth muscle cell response. *Biomaterials* **2005**, *26*, 3123−3129.
(28) Li, S.; Severino, F. P.; Ban, J.; Wang, L.; Pinato, G.; Torre, V. Y.; Chen, Y. Improved neuron culture using scaffolds made of three-dimensional PDMS micro-lattices. *Biomed. Mater.* **2018**, *13*, 034105.
(29) Alameda, M. T.; Osorio, M.; Pedraz, P.; Rodríguez, I. Mechano-Dynamic Analysis of the Bactericidal Activity of Bioinspired Moth-Eye Nanopatterned Surfaces. *Adv. Mater. Interfac.* **2022**, *9*, 2200608.
(30) Li, W.; Tang, Q. Y.; Jadhav, A. D.; Narang, A.; Qian, W. X.; Shi, P.; Pang, S. W. *Sci. Rep.* **2015**, *5*, 1−8.
(31) Jiménez, E.; Mikuszeit, M.; Cuñado, J. L. F.; Perna, P.; Pedrosa, J.; Maccariello, D.; Rodrigo, C.; Niño, M. A.; Bollero, A.; Camarero, J.; Miranda, R. Vectorial Kerr magnetometer for simultaneous and quantitative measurements of the in-plane magnetization components. *Rev. Sci. Instr.* **2014**, *85*, 053904.
(32) Usmani, S.; Aurand, E. R.; Medelin, M.; Fabbro, A.; Scaini, D.; Laishram, J.; Rosselli, F. B.; Ansuini, A.; Zoccolan, D.; Scarselli, M.; De Crescenzi, M.; Bosi, S.; Prato, M.; Ballerini, L. *Sci. Adv.* **2016**, *2*, No. e1600087.
(33) Giacco, V.; Panattoni, G.; Medelin, M.; Bonechi, E.; Aldinucci, A.; Ballerini, C.; Ballerini, L. Cytokine inflammatory threat, but not LPS one, shortens GABAergic synaptic currents in the mouse spinal cord organotypic cultures. *J. Neuroinflammation* **2019**, *16*, 127.
(34) Usmani, S.; Franceschi Biagioni, A. F.; Medelin, M.; Scaini, D. R.; Casani, E. R.; Aurand, D.; Padro, A.; Egimendia, P.; Ramos Cabrer, M.; Scarselli, M.; De Crescenzi, M.; Prato, L.; Ballerini, L. Functional rewiring across spinal injuries via biomimetic nanofiber scaffolds. *Proc. Natl. Acad. Sci. U.S.A.* **2020**, *117*, 25212−25218.
(35) Calaresu, I.; Hernandez, J.; Rauti, R.; Rodilla, B. L.; Arché-Núñez, A.; Perez, L.; Camarero, J.; Miranda, R.; González, M. T.; Rodríguez, I.; Scaini, D.; Ballerini, L. Polystyrene Nanopillars with Inbuilt Carbon Nanotubes Enable Synaptic Modulation and Stimulation in Interfaced Neuronal Networks. *Adv. Mater. Interfaces* **2021**, *8*, 2002121.
(36) Henriksen, A.; Dalslet, B. T.; Skieller, D. H.; Lee, K. H.; Okkels, F.; Hansen, M. F. Planar Hall effect bridge magnetic field sensors. *App. Phys. Lett.* **2010**, *97*, 013507.
(37) Perna, P.; Rodrigo, C.; Jiménez, E.; Teran, F. J.; Mikuszeit, N.; Méchin, L.; Camarero, J.; Miranda, R. *J. App. Phys.* **2011**, *110*, 031919.
(38) Chavent, A.; Iurchuk, V.; Tillie, L.; Bel, Y.; Lamard, N.; Vila, L.; Ebels, U.; Sousa, R. C.; Dieny, B.; di Pendina, G.; Prenat, G.; Langer, J.; Wrona, J.; Prejbeanu, I. L. A multifunctional standardized magnetic tunnel junction stack embedding sensor, memory and oscillator functionality. *J. Magn. Magn. Mater.* **2020**, *505*, 166647.
(39) Sun, X.; Jiang, L.; Pong, P. Magnetic flux concentration at micrometer scale. *Microelectron. Eng.* **2013**, *111*, 77−81.
(40) Ramsden, E. Hall-Effect Sensors, *Practical Transducers*; Edward, R., Ed.; Newnes, 2006; pp 11−33, Chapter 2.
(41) Murzin, D.; Mapps, D. J.; Levada, K.; Belyaev, V.; Omelyanchik, A.; Panina, L.; Rodionova, V. Ultrasensitive Magnetic Field Sensors for Biomedical Applications. *Sensors* **2020**, *20*, 1569.

https://doi.org/10.1021/acsbiomaterials.2c01147
ACS Biomater. Sci. Eng. 2023, 9, 1020−1029

(42) Granell, P. N.; Wang, G.; Cañon Bermudez, G. S.; Kosub, T.; Golmar, F.; Steren, L.; Fassbender, J.; Makarov, D. *NPJ Flex. Electron.* **2019**, *3*, 3.
(43) Fabbro, A.; Villari, A.; Laishram, J.; Scaini, D.; Toma, F. M.; Turco, A. M.; Prato, L.; Ballerini, L. Spinal Cord Explants Use Carbon Nanotube Interfaces To Enhance Neurite Outgrowth and To Fortify Synaptic Inputs. *ACS Nano* **2012**, *6*, 2041−2055.

https://doi.org/10.1021/acsbiomaterials.2c01147
ACS Biomater. Sci. Eng. 2023, 9, 1020−1029